

BigBrain: An Ultrahigh-Resolution 3D Human Brain Model

Katrin Amunts *et al.*

Science 340, 1472 (2013);

DOI: 10.1126/science.1235381

This copy is for your personal, non-commercial use only.

If you wish to distribute this article to others, you can order high-quality copies for your colleagues, clients, or customers by [clicking here](#).

Permission to republish or repurpose articles or portions of articles can be obtained by following the guidelines [here](#).

The following resources related to this article are available online at www.sciencemag.org (this information is current as of September 17, 2013):

Updated information and services, including high-resolution figures, can be found in the online version of this article at:

<http://www.sciencemag.org/content/340/6139/1472.full.html>

Supporting Online Material can be found at:

<http://www.sciencemag.org/content/suppl/2013/06/19/340.6139.1472.DC1.html>

<http://www.sciencemag.org/content/suppl/2013/06/20/340.6139.1472.DC2.html>

A list of selected additional articles on the Science Web sites **related to this article** can be found at:

<http://www.sciencemag.org/content/340/6139/1472.full.html#related>

This article **cites 36 articles**, 12 of which can be accessed free:

<http://www.sciencemag.org/content/340/6139/1472.full.html#ref-list-1>

This article appears in the following **subject collections**:

Neuroscience

<http://www.sciencemag.org/cgi/collection/neuroscience>

BigBrain: An Ultrahigh-Resolution 3D Human Brain Model

Katrin Amunts,^{1,2,3,4*} Claude Lepage,⁵ Louis Borgeat,⁶ Hartmut Mohlberg,^{1,2} Timo Dickscheid,^{1,2} Marc-Étienne Rousseau,⁵ Sébastien Bludau,^{1,2} Pierre-Louis Bazin,⁷ Lindsay B. Lewis,⁵ Ana-Maria Oros-Peusquens,^{1,2} Nadim J. Shah,^{1,2} Thomas Lippert,⁸ Karl Zilles,^{1,2,3,4} Alan C. Evans⁵

Reference brains are indispensable tools in human brain mapping, enabling integration of multimodal data into an anatomically realistic standard space. Available reference brains, however, are restricted to the macroscopic scale and do not provide information on the functionally important microscopic dimension. We created an ultrahigh-resolution three-dimensional (3D) model of a human brain at nearly cellular resolution of 20 micrometers, based on the reconstruction of 7404 histological sections. "BigBrain" is a free, publicly available tool that provides considerable neuroanatomical insight into the human brain, thereby allowing the extraction of microscopic data for modeling and simulation. BigBrain enables testing of hypotheses on optimal path lengths between interconnected cortical regions or on spatial organization of genetic patterning, redefining the traditional neuroanatomy maps such as those of Brodmann and von Economo.

Brain organization on multiple scales and regional segregation are key elements for the development of a realistic model of the human brain. Multiscale organization requires the integration of both multilevel and multimodal data, at the level of cells with their specific connectivity to the level of cognitive systems and the whole brain. Magnetic resonance imaging (MRI) enables the study of the structure and function of the living human brain, with a spatial resolution in the range of 1 mm for structural imaging and somewhat larger for functional MRI (1, 2). This resolution is well above the cellular scale but has been sufficient for establishing human brain atlases to capture information at the level of brain areas, subcortical nuclei, gyri, and sulci (2–5). Cytoarchitectonic probabilistic maps enable the identification of microstructural correlates involved in a specific brain function, as determined by functional MRI, during a cognitive task, for example (6, 7). This approach is supported by combined physiological and imaging studies showing that the response properties of neurons change at the border of two areas (8, 9). Existing human brain atlases do not allow for the integration of information at the level of cortical layers, columns, microcircuits, or cells (fig. S1), such as has been shown recently for mouse or invertebrate brains (10, 11). Still, fine-grain anatomical resolution is a necessary prerequisite to fully understand the

neurobiological basis of cognition, language, emotions, and other processes, as well as to bridge the gap between large-scale neural networks and local circuitry within the cerebral cortex and subcortical nuclei.

We sought to create a human brain model at nearly cellular resolution by going considerably beyond the 1-mm resolution of presently available atlases, taking advantage of recent progress in computing capacities, image analysis, and relying on our experience in processing his-

topological sections of the complete brain. Major challenges include, but are not limited to, the highly folded cerebral cortex, the large number of areas, considerable variability among brains, and the sheer size of the brain, with its nearly 86 billion neurons and the same number of glial cells (12, 13). Compared with rodent or invertebrate brains, the human brain is extremely complex: For example, the volume of a human cerebral cortex is ~7500 times larger than a mouse cortex, and the amount of white matter is 53,000 times larger in humans than in mice. The recently published data set of the digitized mouse brain with 1-μm resolution has a total amount of uncompressed volume data of 8 Tbyte (10). The creation of a volume with similar spatial resolution for the human brain would result in ~21,000 Tbyte. The interactive exploration (as opposed to simple storage) of such a data set is beyond the capacities of current computing. Thus, among other methodological problems, data processing becomes a major challenge for any project aiming at the reconstruction of a human brain at cellular resolution.

To create the brain model, we used a large-scale microtome to cut a complete paraffin-embedded brain (65-year-old female) coronally (Fig. 1), and we then acquired 7400 sections at 20-μm thickness and stained them for cell bodies (14). Histological sections were digitized, resulting in images of maximally 13,000 by 11,000 pixels (10-by-10-μm pixel size). The total volume of this

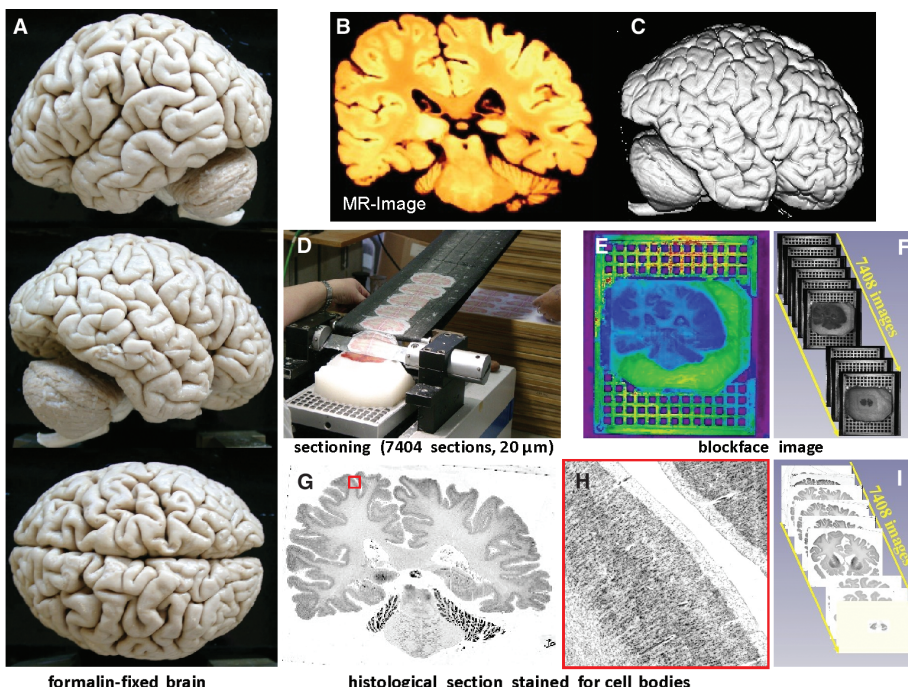


Fig. 1. Illustration of tissue and image processing. (A) Photographs of the fixed brain. Lateral left (top), lateral right (middle), and dorsal (bottom) views. (B) Magnetic resonance image (coronal view) and (C) 3D-reconstructed MRI volume of the fixed brain. (D) Histological sectioning. (E) Blockface image of a section (pseudocolored) resting on the mounting grid that served for alignment of the blockface images. (F) Series of blockface images. (G) Cell body–stained histological sections with the region of interest denoted by a red box. This area is shown with higher magnification in (H). (I) Series of histological images, which were 3D-reconstructed using the blockface images (F) and the MRI (C).

¹Institute of Neuroscience and Medicine (INM-1, INM-4), Research Centre Jülich, D-52425 Jülich, Germany. ²Jülich-Aachen Research Alliance (JARA), Translational Brain Medicine, Jülich, Germany. ³Section Structural-Functional Brain Mapping, Department of Psychiatry, Psychotherapy and Psychosomatics, RWTH Aachen University, Pauwelstrasse 30, D-52074 Aachen, Germany. ⁴C. and O. Vogt Institute for Brain Research, Heinrich Heine University Düsseldorf, D-40001 Düsseldorf, Germany. ⁵Montreal Neurological Institute (MNI), McGill University, Montreal, Canada. ⁶National Research Council of Canada, Ottawa, Canada. ⁷Max Planck Institute for Human Cognitive and Brain Sciences, D-04103 Leipzig, Germany. ⁸Jülich Supercomputing Centre (JSC), Research Centre Jülich, D-52425 Jülich, Germany.

*Corresponding author. E-mail: k.amunts@fz-juelich.de

data set was 1 Tbyte. The uninterrupted data acquisition time was ~1000 hours. To generate a data set with isotropic resolution, we down-scaled all images to 20 μm by 20 μm to match the section thickness of 20 μm .

Histological processing inevitably introduces artifacts, which pose problems at all stages of the three-dimensional (3D) reconstruction process. Defects include rips, tears, folds, missing and displaced pieces, distortion (shear), stain inhomogeneity, and crystallization. We performed both manual and automatic repairs to restore the integrity of all sections before the 3D reconstruction of the whole brain as a contiguous volume (figs. S2 to S4). The repaired sections were registered to the MRI, which served as an undistorted frame of reference, and further aligned section-to-section with the use of nonlinear registration. All calculations were carried out on high-performance computing (HPC) facilities within the Compute Canada network and were run on Jülich Research on Petaflop Architecture (JUROPA) at the Jülich Supercomputing Centre (see the supplementary materials).

Figure 2 shows three example regions from primary sensory and motor cortices in the original coronal plane and the reconstructed sagittal and horizontal planes. Note the smooth contours

in the virtual sections, confirming the high quality of the 3D reconstruction. The images in all three planes at 20 μm reveal differences in the laminar pattern between brain areas and enable an observer-independent definition of borders between them (15). To prove the feasibility of our mapping approach in higher associative cortices with more subtle architectonic differences in between, we defined a border between Brodmann area (BA) 10 of the frontal pole and BA32 (Fig. 3). Although some artifacts due to residual mismatches between aligned sections still exist, the border of interest has been detected in the original and the horizontal virtual plane at the identical location. Thus, the present “BigBrain” model allows the recognition of not only the borders between primary cortical areas [feasible, at least to some extent with advanced MRI technology (16–19)], but also between higher associative areas. Until now, the recognition of the latter borders, based on their laminar pattern, was accessible in 2D histological sections and light-microscope images, but at only those locations where the cortex was cut orthogonal to the pial surface. The latter condition is often not fulfilled (e.g., Fig. 2A, coronal), thus making border definition based on quantitative criteria throughout the whole cortical ribbon in 2D sections impossible.

The 3D-analysis indicates that the relationship between cortical folds and borders of cytoarchitectonic areas is heterogeneous. Whereas this relationship is considerably close for some areas, it seems to be less well defined for others. For example, the border between the primary motor and somatosensory cortex is localized in the fundus of the central sulcus, independently from the orientation of the cutting plane (Fig. 2A). This is not the case for the primary auditory area Te1 (BA41), which is more or less restricted by Heschl’s gyrus in two planes (Fig. 2C), but has no sulcal landmark in the third plane (20). Whereas the sulcal pattern is associated with areal borders in other, nonprimary areas [for example, BA35 (21)], the border between the primary visual area BA17 (V1) and neighboring 18 (V2) (Fig. 2B) does not seem to be related to a sulcus. The same is true for the border between BA10 and the neighboring cingulate cortex (Fig. 3). This variable relationship between cytoarchitectonic borders and macroscopic landmarks has been analyzed in the past (22, 23), but not in 3D space.

The spatial dimension, however, is relevant, because the directionality of hemispheric growth during embryonic and fetal development and the coupling of cortical areas via fiber tracts define the spatial organization of cortical areas and their connections, as well as sulci and gyri in the adult brain. The effect of early cortical regionalization on folding has been modeled by introducing geometric, mechanic, and growth asymmetries in the model (24). Another model considered variability between brains during ontogeny (25). A recent study has emphasized the strong geometric structure of fibers and pathways as a result of early development (26). Another study reported that fiber connection patterns closely follow gyral folding patterns in the direction tangential to the cortical sphere (27). The concept of the tension-based morphogenesis effect provides a theory of folding processes caused by the tension of fiber tracts connecting brain regions (28, 29), whereas others identify differences in the relationship between supra- and infragranular layers (i.e., cytoarchitectonic differences) as factors shaping cortical folding (30). The validation of all these concepts requires high-resolution spatial models of the human brain for testing the underlying hypotheses.

The present findings and data on the localization of cortical areas with respect to gyri and sulci support the notion that their topographical relationship is not merely a pure geometric phenomenon, but rather the result of an interference of developmental processes and the internal structure of areas, including their connectivity (31). A systematic analysis of cortical borders across the whole cortical ribbon is mandatory. The variability in this relationship across individuals requires the generation of additional BigBrain data sets in the future, labor-intensive work that is currently underway.

To consider intersubject variability in the present data set, vector fields have been calculated

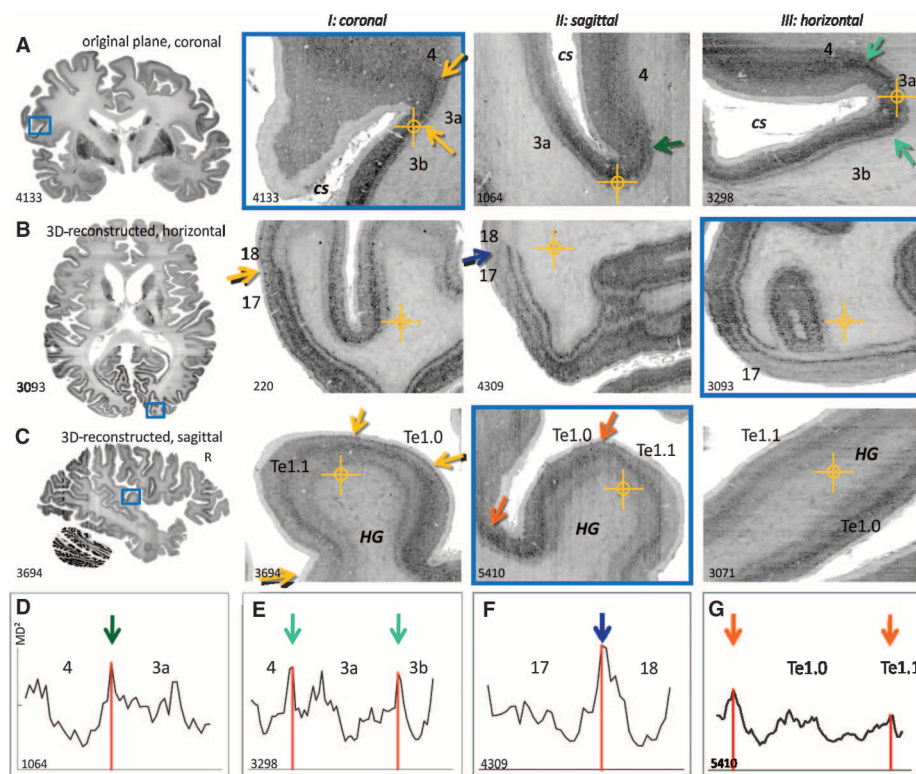


Fig. 2. Primary cortical regions in the three planes of section. (A) Sensorimotor (BA4, 3a and 3b), (B) visual [BA17 (V1) and BA18 (V2)], and (C) auditory cortex (areas Te1.0, Te1.1 as part of BA41) (left column). Overviews of the whole-brain sections in the original plane (A) and the 3D-reconstructed horizontal (B) and sagittal (C) planes. Crosshairs denote identical positions within a row. Columns I to III show coronal, sagittal, and horizontal planes, respectively. cs, central sulcus; HG, Heschl’s gyrus. Section numbers are shown in the lower-left corner of each panel. (D to G) Definition of borders for regions of interest from (A) to (C), based on the Mahalanobis distance (15). Corresponding borders are labeled by identically colored arrows (see also supplementary materials and Fig. 3).

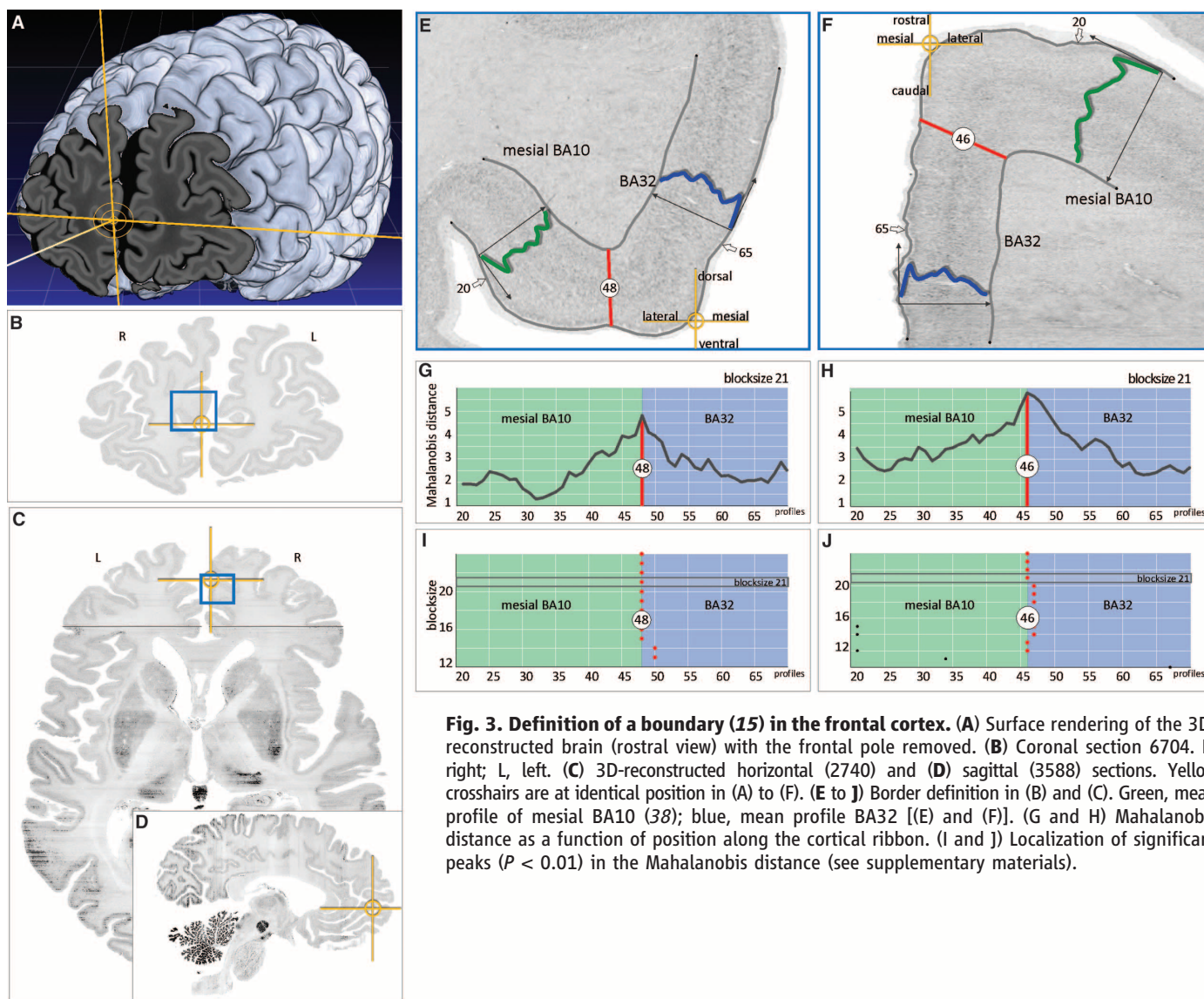


Fig. 3. Definition of a boundary (15) in the frontal cortex. (A) Surface rendering of the 3D-reconstructed brain (rostral view) with the frontal pole removed. (B) Coronal section 6704. R, right; L, left. (C) 3D-reconstructed horizontal (2740) and (D) sagittal (3588) sections. Yellow crosshairs are at identical position in (A) to (F). (E to J) Border definition in (B) and (C). Green, mean profile of mesial BA10 (38); blue, mean profile BA32 [(E) and (F)]. (G and H) Mahalanobis distance as a function of position along the cortical ribbon. (I and J) Localization of significant peaks ($P < 0.01$) in the Mahalanobis distance (see supplementary materials).

based on a 400- μm isotropic down-sampled volume, to define a homeomorphic transformation between the BigBrain and the Montreal Neurological Institute (MNI) space (see supplementary materials). Thus, cytoarchitectonic or functional probability maps in MNI space, which embeds information about intersubject variability, can be mapped to the BigBrain data set. We plan to establish links to other reference systems so as to combine high-resolution cytoarchitectonic data with, for example, gene-expression maps (32), neural projections (33) or future brain-activity maps (34).

The BigBrain data set will be made publicly available to promote the development of new tools for defining 3D cytoarchitectonic borders (<http://bigbrain.cbrain.mcgill.ca>). BigBrain allows the extraction of parameters of cortical organization by enabling measurements parallel to cell columns (e.g., cortical thickness, densities of cell bodies per column, surface measures) to pro-

vide a “gold standard” for calibrating *in vivo* measurements of cortical thickness and other measures.

The BigBrain data set represents a new reference brain, moving from a macroanatomical perspective to microstructural resolution. This model provides a basis for addressing stereotaxic and topological positions in the brain at micrometer range (e.g., with respect to cortical layers and sublayers). BigBrain will make it possible to localize findings obtained in cellular neuroscience and mapping studies targeting transmitter receptor distributions (35), fiber bundles (36), and genetic data (32, 37). The BigBrain model can also be exploited as a source for generating realistic input parameters for modeling and simulation. It thus represents a reference frame with nearly cellular resolution, a capability that has not been previously available for the human brain, while considering the regional heterogeneity of human brain organization.

References and Notes

1. P. E. Roland, K. Zilles, *Trends Neurosci.* **17**, 458 (1994).
2. A. W. Toga, P. M. Thompson, S. Mori, K. Amunts, K. Zilles, *Nat. Rev. Neurosci.* **7**, 952 (2006).
3. A. C. Evans, A. L. Janke, D. L. Collins, S. Baillet, *Neuroimage* **62**, 911 (2012).
4. P. E. Roland *et al.*, *Hum. Brain Mapp.* **1**, 173 (1993).
5. J. Talairach, P. Tournoux, *Coplanar Stereotaxic Atlas of the Human Brain* (Thieme, Stuttgart, Germany, 1988).
6. K. Zilles, K. Amunts, *Nat. Rev. Neurosci.* **11**, 139 (2010).
7. S. B. Eickhoff, S. Hein, K. Zilles, K. Amunts, *Neuroimage* **32**, 570 (2006).
8. K. Nelissen, G. Luppino, W. Vanduffel, G. Rizzolatti, G. A. Orban, *Science* **310**, 332 (2005).
9. G. Luppino, M. Matelli, R. M. Camarda, V. Gallesse, G. Rizzolatti, *J. Comp. Neurol.* **311**, 463 (1991).
10. A. Li *et al.*, *Science* **330**, 1404 (2010).
11. H. Peng, Z. Ruan, F. Long, J. H. Simpson, E. W. Myers, *Nat. Biotechnol.* **28**, 348 (2010).
12. S. Herculano-Houzel, *Proc. Natl. Acad. Sci. U.S.A.* **109** (suppl. 1), 10661 (2012).
13. C. C. Hilgetag, H. Barbas, *Brain Struct. Funct.* **213**, 365 (2009).
14. B. Merker, *J. Neurosci. Methods* **9**, 235 (1983).
15. A. Schleicher, P. Morosan, K. Amunts, K. Zilles, *J. Autism Dev. Disord.* **39**, 1568 (2009).

16. R. M. Sánchez-Panchuelo, S. T. Francis, D. Schluppeck, R. W. Bowtell, *J. Magn. Reson. Imaging* **35**, 287 (2012).
17. G. M. Fatterpekar *et al.*, Cytarchitecture of the human cerebral cortex: MR microscopy of excised specimens at 9.4 tesla. *Am. J. Neurorad.* **23**, 1313 (2002).
18. M. F. Glasser, D. C. Van Essen, *J. Neurosci.* **31**, 11597 (2011).
19. N. B. Walters *et al.*, *Hum. Brain Mapp.* **28**, 1 (2007).
20. P. Morosan *et al.*, *Neuroimage* **13**, 684 (2001).
21. J. C. Augustinack *et al.*, *Neuroimage* **64**, 32 (2013).
22. K. Amunts *et al.*, *Neuroimage* **22**, 42 (2004).
23. B. Fischl *et al.*, *Cereb. Cortex* **18**, 1973 (2008).
24. R. Toro *et al.*, *Cereb. Cortex* **18**, 2352 (2008).
25. J. Lefèvre, J. F. Mangin, *PLoS Comput. Biol.* **6**, e1000749 (2010).
26. V. J. Wedeen *et al.*, *Science* **335**, 1628 (2012).
27. H. Chen *et al.*, Coevolution of gyral folding and structural connection patterns in primate brains. *Cereb. Cortex* **23**, 1208 (2013).
28. D. C. Van Essen, *Nature* **385**, 313 (1997).
29. A. Kriegstein, S. Noctor, V. Martínez-Cerdeño, *Nat. Rev. Neurosci.* **7**, 883 (2006).
30. E. Armstrong *et al.*, *Cereb. Cortex* **1**, 426 (1991).
31. K. Zilles, K. Amunts, *Science* **335**, 1582 (2012).
32. A. R. Jones, C. C. Overly, S. M. Sunkin, *Nat. Rev. Neurosci.* **10**, 821 (2009).
33. N. Kasthuri, J. W. Lichtman, *Nat. Methods* **4**, 307 (2007).
34. A. P. Alivisatos *et al.*, *Science* **339**, 1284 (2013).
35. K. Zilles, K. Amunts, *Curr. Opin. Neurobiol.* **22**, 331 (2009).
36. M. Axer *et al.*, High-resolution fiber tract reconstruction in the human brain by means of three-dimensional polarized light imaging (3D-PLI). *Front. Neuroinform.* **5**, 34 (2011).
37. E. H. Shen, C. C. Overly, A. R. Jones, *Trends Neurosci.* **35**, 711 (2012).
38. S. Bludau *et al.*, *NeuroImage* **10.1016/j.neuroimage**, 2013.05.052 (2013).

Acknowledgments: We acknowledge funding support from Canada's Advanced Research and Innovation Network (CANARIE; www.canarie.ca) for the software development of the CBRAIN portal. We also thank Compute Canada (www.computecanada.ca) for continued support through

extensive access to the Compute Canada HPC grid. We thank P. Morosan and U. Pietrzik for helpful discussion, as well as F. Kocae and U. Blohm for technical assistance. We are particularly grateful to R. Adalat for his efforts in management and coordination on this collaboration. This work was supported by the Portfolio project "Supercomputing and Modeling for the Human Brain," funded by the Helmholtz Association Germany, and the Human Brain Project, a European Union Flagship project. The normalized BigBrain data are available at: <http://bigbrain.cbrain.mcgill.ca> (upon free subscription).

Supplementary Materials

www.sciencemag.org/cgi/content/full/340/6139/1472/DC1

Materials and Methods

Figs. S1 to S6

References

Movie S1

21 January 2013; accepted 15 May 2013

10.1126/science.1235381

Compartmentalized Calcium Transients Trigger Dendrite Pruning in *Drosophila* Sensory Neurons

Takahiro Kanamori,¹ Makoto I. Kanai,¹ Yusuke Dairyo,^{1,3} Kei-ichiro Yasunaga,¹ Rei K. Morikawa,¹ Kazuo Emoto^{1,2*}

Dendrite pruning is critical for sculpting the final connectivity of neural circuits as it removes inappropriate projections, yet how neurons can selectively eliminate unnecessary dendritic branches remains elusive. Here, we show that calcium transients that are compartmentalized in specific dendritic branches act as temporal and spatial cues to trigger pruning in *Drosophila* sensory neurons. Calcium transients occurred in local dendrites at ~3 hours before branch elimination. In dendritic branches, intrinsic excitability increased locally to activate calcium influx via the voltage-gated calcium channels (VGCCs), and blockade of the VGCC activities impaired pruning. Further genetic analyses suggest that the calcium-activated protease calpain functions downstream of the calcium transients. Our findings reveal the importance of the compartmentalized subdendritic calcium signaling in spatiotemporally selective elimination of dendritic branches.

Nervous system development relies on a balance between progressive and regressive events (1, 2). After progressive events such as axon and/or dendrite outgrowth and synapse formation, neurons refine their connections through regressive events, such as pruning of axons and dendrites (1–3). In dendrite pruning, neurons selectively eliminate excessive or inappropriate connections that formed during development. Thus, proper dendrite pruning depends on local activation of the machinery needed to eliminate unnecessary dendritic branches; however, our understanding of locally acting mechanisms involved in this process remains incomplete.

Drosophila dendrite arborization sensory neurons are classified into four subtypes (I to IV) on

the basis of their dendritic morphology, and class IV dendrite arborization (C4da) sensory neurons undergo dendrite pruning during early metamorphosis (3–7). C4da dendrites are typically severed at the proximal regions ~5 hours after puparium formation (APF), followed by fragmentation and clearance of the severed branches by 14 hours APF (4, 5). Previous studies have demonstrated that the ubiquitin-proteasome system and the caspase activity act to execute the pruning process (5–7), but it remains unclear what mechanisms locally determine which dendritic branches are to be eliminated.

Calcium signaling is often utilized for the spatiotemporal regulation of neural development (2, 3). To monitor changes in intracellular Ca^{2+} ion concentration ($[\text{Ca}^{2+}]_i$), we expressed the genetically encoded calcium (Ca^{2+}) indicator GCaMP3 selectively in C4da neurons using the Gal4/UAS binary system (which exploits the yeast Gal4 transcriptional activator and the upstream activating sequence) (fig. S1) (8). We continuously monitored $[\text{Ca}^{2+}]_i$ levels in single C4da neurons from 1 to 8 hours APF and found no apparent $[\text{Ca}^{2+}]_i$

changes in soma and axons (9). However, we observed robust Ca^{2+} transients in groups of dendrites, which typically started 2 to 4 hours APF (Fig. 1, A to C, and movie S1). The dendritic Ca^{2+} transients appeared with a frequency of $0.88 \pm 0.66 \text{ min}^{-1}$ on average ($n = 36$), and the mean change in fluorescence ($\Delta F/F_0$) of these events was $499.1 \pm 162.5\%$ (99 events, $n = 10$). Once Ca^{2+} transients commenced in a particular group of dendrites, transients continued to occur in the same dendrites. Furthermore, patterns, as well as amplitudes, of Ca^{2+} transients observed in individual dendritic groups were not correlated to each other (Fig. 1D and movie S1), which suggested that the Ca^{2+} transients are compartmentalized into each subdendritic region. Hereafter, we designate the groups of dendritic branches with the compartmentalized Ca^{2+} transients as "branch units." Dendritic arbors in single neurons were typically subdivided into 4 to 5 branch units, which were mainly formed in dendrites distal from the secondary and from the tertiary branches (fig. S2).

An example of long-term simultaneous monitoring of $[\text{Ca}^{2+}]_i$ and dendritic arbor structures by GCaMP3 and membrane-bound red fluorescent protein (RFP), respectively, is shown (Fig. 2). The first branch unit started its Ca^{2+} transients 2 hours APF, when no obvious pruning was detected (Fig. 2, C and D, and movie S2). The second and third branch units started their Ca^{2+} transients around 3.5 and 4.5 hours APF, respectively, when all the dendritic branches seemed still intact (Fig. 2E and movies S3 and S4). Five hours APF, the first branch unit underwent fragmentation after a continuous Ca^{2+} influx, whereas the other two still continued their Ca^{2+} transients, and their dendritic arbors seemed intact (Fig. 2F). Similarly, the second and third branch units were eliminated after continuous Ca^{2+} influx about 6.5 and 7.5 hours APF, respectively (Fig. 2, G and H). Thus, dendrites are pruned in the temporal order in which they experienced Ca^{2+} transients, the mean duration of which was $140.5 \pm 43.6 \text{ min}$ ($n = 11$). The location and timing of the occurrence of Ca^{2+} transients correlated perfectly with those of dendrite pruning ($n \geq 50$ neurons),

¹Department of Cell Biology, Osaka Bioscience Institute, 6-2-4 Furuedai, Suita, Osaka 565-0872, Japan. ²Department of Biological Sciences, Graduate School of Science, The University of Tokyo, 7-3-1 Hongo, Bunkyo-ku, Tokyo 113-0033, Japan. ³Graduate School of Biological Sciences, Nara Institute of Science and Technology, 8916-5 Takayama, Ikoma, Nara 630-0192, Japan.

*Corresponding author. E-mail: emoto@biol.s.u-tokyo.ac.jp